Title

Time resolved 3D momentum imaging of ultrafast dynamics by coherent VUV-XUV radiation

Journal

Review of Scientific Instruments, 87(6)

ISSN

0034-6748

Authors

Sturm, FP

Wright, TW

Ray, D

et al.

Publication Date

2016-06-01

DOI

10.1063/1.4953441

Peer reviewed

Time Resolved 3D Momentum Imaging of Ultrafast Dynamics by Coherent VUV-XUV Radiation

F. P. Sturm,[1, 2, a)] T. W. Wright,[1] D. Ray,[1] I. Zalyubovskaya,[1] N. Shivaram,[1] D. Slaughter,[1] P. Ranitovic,[1, 3] A. Belkacem,[1] and Th. Weber[1]

[1)] *Ultrafast X-Ray Science Lab, Lawrence Berkeley National Laboratory, Berkeley, CA 94720, USA*

[2)] *Institut für Kernphysik, Universität Frankfurt, Max-von-Laue Str. 1, D-60438 Frankfurt, Germany*

[3)] *ELI-ALPS, ELI-Hu Nkft, Dugonics ter 13, Szeged H6720, Hungary*

(Dated: 14 February 2016)

We present a new experimental setup for measuring ultrafast nuclear and electron dynamics of molecules after photo-excitation and ionization. We combine a high flux femtosecond vacuum ultraviolet (VUV) and extreme ultraviolet (XUV) source with a cold molecular beam and a 3D-momentum imaging particle spectrometer to measure electrons and ions in coincidence. We describe a variety of tools developed to perform pump-probe studies in the VUV-XUV spectrum and to modify and characterize the photon beam. First benchmark experiments are presented to demonstrate the capabilities of the system.

PACS numbers: 33.80.-b,42.65.Ky,82.53.Kp

[a)] fpsturm@lbl.gov

I. INTRODUCTION

Over the past decades, molecular spectroscopy using light sources has yielded rich information about molecular structure, electronic states, and electronic transitions in photo excited systems. Synchrotron rings are excellent sources for such studies due to their large photon energy range, good spectral selectivity, high brightness, and high repetition rate. However, the pulse length of synchrotron sources ($\sim$ 50 to 100 ps) does not allow for studying the ultrafast transient dynamics in molecular systems such as geometrical changes or electron dynamics in molecules in the time domain. Nuclear dynamic evolves on femtosecond timescales and is of great importance in nature as it allows for an efficient energy transfer from electrons to the underlying molecular structure. This is evident especially in triatomic and even more complex molecules without compromising their stability. Examples have been found in a variety of systems such as in the photosynthesis of plants[1], in vision[2], or in the photo-protection of the skin[3]. In order to study nuclear dynamics in real-time, involving non-Born-Oppenheimer processes that couple electronic and nuclear motion, light sources providing ultrashort pulses of femtosecond duration are required.

Light sources producing coherent ultrashort pulses of 10s of femtoseconds have been developed over the past 30 years enabling time-resolved measurements with pump-probe schemes. Crystals, such as Ti:Sapphire, that emit in the infrared spectrum are commonly used to obtain the bandwidth needed to support a pulse in the femtosecond time domain. However, the ionization potential of molecules is on the order of several eV, hence, the absorption of multiple infrared photons is required for ionization. This can be achieved by exposing the molecule to a strong laser field ($> 10^{12}\, W/cm^2$). Such laser induced fields are comparable to the electric field between nuclei and electrons in the molecule and can therefore distort or "dress" the electronic states. Hence, this spectroscopy method does not allow for observing a molecule in its natural unperturbed regime but instead in a dressed state, imposed by the strong laser field. In order to observe highly excited electronic states of the unperturbed molecule, photons of sufficient energy are needed.

High Harmonic Generation (HHG) and Free Electron Lasers (FELs) are the prominent techniques producing ultrafast pulses of coherent photons beyond the vacuum-ultraviolet spectrum that are required for accessing the majority of (highly) exited neutral and singly ionized states of molecules. In FELs, compressed electron bunches are sent through a series

of undulators stimulating coherent emission of photons. Very high flux photon beams at photon energies up to several keV can be obtained[4–6]. However, the pulse length is limited by space charge effects of the electron bunches, and only few facilities use laser seeding to ensure stable photon beam conditions. This complicates the combination of FELs with lasers systems necessary for studying VUV excitation as well as two color measurements.

High Harmonic Generation, on the other hand, is a well-established technique to produce ultrashort pulses in a laboratory setting[7,8]. In the most common scheme, a strong linearly polarized laser field tunnel ionizes the atoms in a noble gas and drives the electrons according to the sinusoidal electromagnetic field of the laser beam. If an electron returns to the vicinity of the parent ion, the electron can recombine with the ion. This results in the emission of a photon with an energy equivalent to the kinetic energy of the electron gained in the driving laser field plus the ionization potential. The photon energies generated in this process are in the vacuum ultraviolet (VUV) and extreme ultraviolet (XUV) and are well suited for the investigation of molecular dynamics in a wide range of systems. For a single color driving field and a symmetric generation medium, the 3-step process of ionization, field driven propagation, and recombination/ photo-emission repeats every half cycle[9]. This creates an attosecond pulse train in the time domain that corresponds to a discrete frequency spectrum of odd harmonics of the fundamental frequency of the driving field up to an energy limit defined by the driving field and the medium[7,10]. Using gating techniques, single attosecond pulses can be generated[11,12].

While the pulse properties are ideal for the investigation of nuclear and even electron dynamics, the conversion efficiency of the HHG in a gas is extremely low (usually $\sim 10^{-5} - 10^{-6}$). This makes it very difficult to obtain a sufficiently intense beam to achieve two-photon absorption in a pump-probe study. As a result, only very few HHG sources produce sufficient flux for multi-photon absorption in the VUV-XUV spectrum. Due to the already challenging laser requirements, these setups usually do not employ complex multi-differential experimental spectroscopy techniques[13,14].

COLd Target Recoil Ion Momentum Spectroscopy (COLTRIMS), also known as "Reaction Microscopy"[15] is a spectroscopy technique that delivers rich information about the electronic states and molecular fragmentation pathways in photoionization reactions. The coincidence measurement of the positions and time-of-flights of the fragment ions and electrons allows for the reconstruction of the 3D-momentum vectors of the particles at the time

of ionization. Detecting the momentum vectors of correlated particles from an ionization event (e.g. electron-ion, ion-ion pairs) is a very powerful method to gain insight into the energetics, ionization mechanisms, and dynamics of the target at hand. Highly differential measurements and even kinematically complete experiments are possible. Coincident particle detection enables the computation of relative quantities, i.e. measurements in the target frame. This gives access to energy correlation maps, e.g. the electron kinetic energy as a function of the kinetic energy release of the recoiling ions, which essentially probes the potential energy surfaces of the target. Measuring the energy of one electron as a function of the energy of a second electron reveals the energy sharing that is characteristic of the ionization mechanism. Moreover, the emission patterns of electrons with respect to the molecular structure can be gained and visualized in so called Molecular Frame Photoelectron Angular Distributions (MFPADs) as long as the axial recoil approximation is valid (the ion emission direction represents the molecular axis at the time of ionization).

Existing experimental setups combining HHG with complex multi-fragment imaging detection schemes usually require the combination of the XUV radiation with a strong field for either the pump or the probe step of the experiment[16–18]. In this work, we present an experimental apparatus that enables coincidence 3D-momentum imaging spectroscopy of atomic and molecular targets in femtosecond time-resolved measurements using pairs of multi-color VUV, XUV and IR pulses. A high flux high harmonics source is combined with a 3D-momentum imaging setup that can record electron and ion 3D-momenta in coincidence. The various components of the XUV beamline as well as the experimental end-station are described in the following section. In Section III, two measurements are shown that showcase the capabilities of our methods. In the last section we will summarize and discuss future developments.

II. EXPERIMENTAL SETUP

Figure 1 shows an overview of the experimental setup built at the Lawrence Berkeley National Laboratory in Berkeley, California. It consists of a high power laser system that generates a high flux of VUV and XUV photons using a gas phase High Harmonics Generation (HHG). The laser system and the technique applied for high flux harmonic generation are described in Section II A. An in-vacuum Split-Mirror Interferometer (SMI) splits the

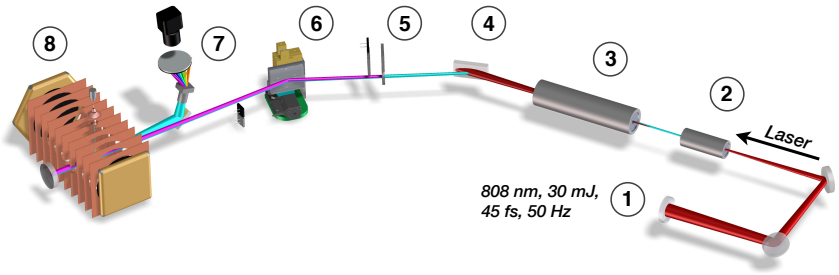

FIG. 1. (color online) Overview of the high harmonics beamline and end-station. The amplified and compressed laser beam (laser system not shown) is loosely focused by using a mirror (f = 6 m) (1) into a 10 cm gas cell (2) filled with a noble gas for High Harmonic Generation (HHG). Also shown are the (3) gas filter cell (see Figure 2), (4) silicon mirror at Brewster's angle (15° grazing anlge), (5) solid filters and diode, (6) Split-Mirror Interferometer (SMI) (see Figure 6), (7) XUV-spectrometer (see Figure 5), and (8) COLTRIMS end-station (see Figure 8).

photon beam into pump and probe arms with both attosecond precision and picosecond delay range (see Section II D). Using a range of gas, glass, and metal filters as well as multi-layer coated mirrors, the beam energy of both the pump and the probe pulses can be selected individually to suit a particular experiment (see Section II B). A custom built compact XUV spectrometer characterizes the photon beam delivered to the target (see Section II C). In Section II E, the COLTRIMS type 3D-momentum imaging end-station is presented.

A. Laser System and High Harmonic Generation

In order to obtain a high XUV photon flux, we use a high power infrared ($\lambda = 808$ nm) laser system delivering pulses of 30 mJ energy with a temporal width of 45 fs at 50 Hz repetition rate.

At high intensities, the harmonic up-conversion is limited by the ionization of the generation medium. Therefore, we distribute the pulse energy by loosely focusing the beam with a curved mirror ($f = 6$ m) into a 10 cm long gas cell while maintaining the intensity at an optimum level of about $2 - 4 \times 10^{14}$ W/cm^2. The resulting large focus maximizes the number of active atoms for High Harmonic Generation (for details see[19],[20]). The phase matching of harmonics generated over the extended focal region is extremely important for

an efficient production of VUV and XUV photons. The gas pressure, the focal position, as well as the compression of the pulses are therefore routinely adjusted to achieve a flux of about 10^9 to 10^{10} photons/ harmonic/ shot). The absolute flux is measured using calibrated photodiodes.

The laser system is based on a KM-Labs Dragon oscillator kit with Ti-Sapphire crystal to create a spectrally broad laser beam centered at 808 nm. The beam is amplified to 60 mJ per pulse at 50 Hz by means of a regenerative amplifier (Coherent Evo 15 pump laser) followed by a homemade 6-pass amplifier (Continuum Powerlite pump laser) and compressed with a matched grating pair. In air, the high pulse energy causes self-phase modulation and other non-linear effects. In a vacuum, the high peak intensity, as well as average power have been observed to damage mirrors and gratings. Therefore, we compress the beam in a helium filled vacuum chamber at 100 Torr pressure which facilitates significant heat exchange by collisions between the room temperature gas and optical surfaces. The beam leaves the helium environment through a thin window (UV fused silica 250 μm) that separates the compression and beam folding chambers from the vacuum beamline containing the gas cell for High Harmonic Generation.

B. Photon Energy Selection

Selecting specific photon energies in order to excite a particular electronic transition can be key for understanding complex molecular dynamics. Moreover, the ability to manipulate the spectral content of the harmonics is crucial for controlling the coupled electron nuclear dynamics triggered by coherent ultrashort pulses. Monochromators based on dispersive gratings can be used to isolate a specific part of the spectrum. However, the use of ultrashort pulses imposes additional challenges as dispersion will stretch the pulse significantly in the time domain. Time-compensated monochromators where the pulses are recompressed with a second grating pair have been developed but come at the cost of a significantly reduced transmission ($\sim$ 10 %) due to the additional optics[21]. Here, we have employed a variety of other methods for spectral selection that are described in the following section. In this setup, we use thin metal filters, glass windows, as well as multilayer coated mirrors to choose a particular subset of the high harmonic spectrum. All filters and foils are mounted on in-vacuum motorized stages for a quick selection of the photon spectrum delivered to

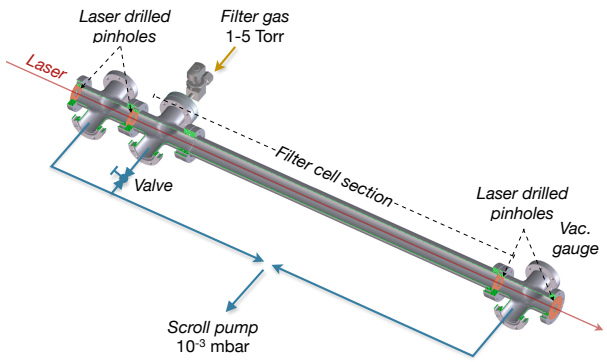

FIG. 2. (color online) Gas filter cell built as a part of the Conflat vacuum beamline (See 3 in Figure 1).

the experiment. D-shaped filters allow for different energies for the pump and probe arms. Additionally, an inline gas cell, shown in Figure 2, was developed for using gases for filtering the harmonic spectrum. The setup consists of CF vacuum tubing that is separated into a 80 cm long cell that can be filled with various filter gases and differentially pumped regions before and after the cell. Before the HHG or gas cell are filled with gas the intense fundamental photons of the laser are employed to drill transmission apertures throughout the assembly

Figure 3 shows an overview of the transmitted spectra measured after the application of various filter materials. The spectra were recorded using the custom build XUV-spectrometer described in Section II C. Gases, shown on the top (a), exhibit good transmission but provide only a course energy selection. Solid filter materials (b) exhibit better selectivity but can significantly reduce the transmission.

Common foil materials are tin, aluminum, and indium. At thicknesses of 0.1 to 0.15 μm, these foils are extremely delicate and oxidization can reduce the transmission significantly, as can be seen in the measured spectra (Figure 3). Windows made of MgF_2 and CaF_2 are good materials for selecting the 3^{rd} and the 5^{th} harmonic of the fundamental frequency while MgF_2 also transmits a small fraction of the 7^{th} harmonic. Dispersion in the material delays the pulse going through the glass and separates different harmonic orders several hundred fs in time. By adjusting the position of the delay stage, time overlap of pump and probe pulses for a specific harmonic can be selected. Meanwhile, the other frequency components are preceding or are delayed sufficiently in time to avoid influence on the experiment. This effect is demonstrated in Figure 4. Here, the high harmonics beam was split into two

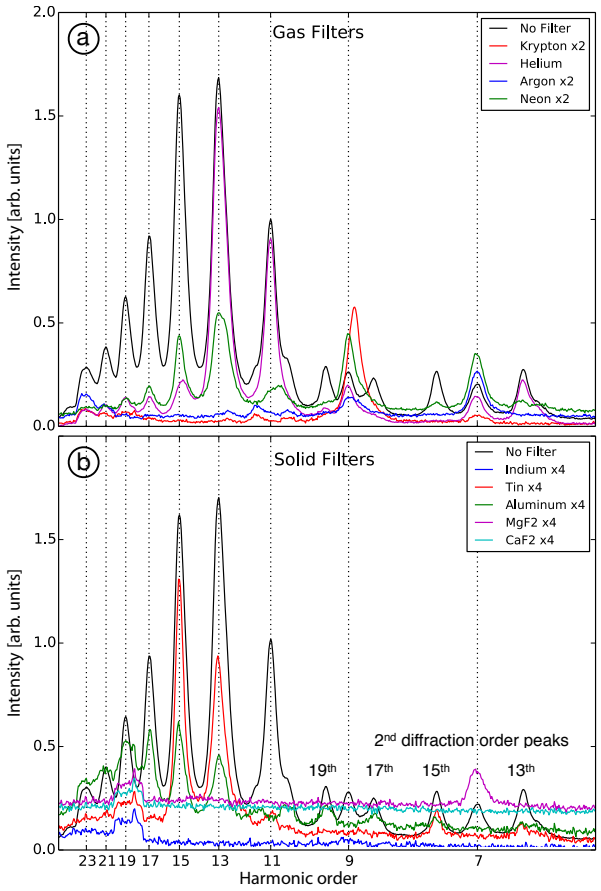

FIG. 3. (color online) XUV spectra of the HHG beam measured after transmission through different gaseous (a) and solid (b) filter materials using the XUV spectrometer.

arms using the Split-Mirror Interferometer (see Section II D) and overlapped spatially into a C_2H_4 gas target in the end-station. A MgF_2 window was inserted into one arm, delaying and separating the harmonics temporally. The signal of $C_2H_4{}^+$ ions was recorded using a boxcar integrator with respect to the temporal delay between the two arms. The delay positions corresponding to the time-overlap of the 5^{th} harmonic (and other orders) with the separated IR, 3^{rd} , and 5^{th} harmonics are marked in the figure. Depending on the window thickness and the initial pulse length, dispersion in the window can be used to compensate for the negative chirp intrinsic to the high harmonic generation process resulting in a shorter pulse. The application of such filters is described in detail elsewhere[22].

The most stringent energy selection without high photon losses (as in monochromators) can usually be achieved by exploiting multilayer coatings on a mirror substrate. The materials of the coating layers, thicknesses, and separations are tailored to the desired wavelength[23].

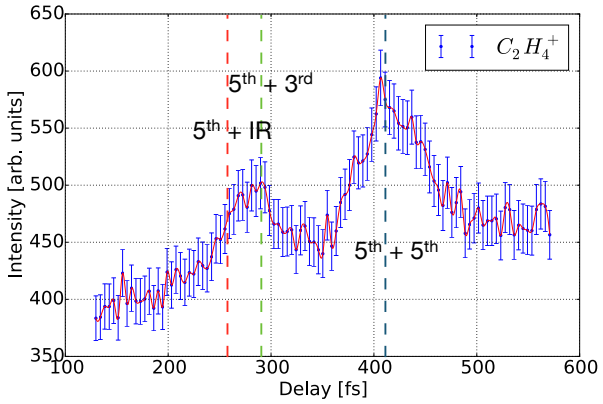

FIG. 4. (color online) $C_2H_4^+$ signal from multi-photon ionization using low order harmonics. Inserting a MgF_2 window into one photon beam arm separates the orders temporally causing selective overlap of the pump and probe pulses depending on the harmonic order and the position of the time delay stage between the two light beams.

We have used a B_4C broadband coating[24] on our final back focusing mirror for the initial experiments. In order to obtain different colors for the pump and probe beams, one can choose to coat each half of the back focusing mirror individually.

C. XUV-Spectrometer

Characterizing the spectral content of the HHG beam is crucial for understanding the complex processes initiated by excitation and ionization using XUV photons. This is particularly challenging when filters and mirrors have to be used instead of monochromators which deliver well defined energies. Thus, we have developed a compact XUV-spectrometer to characterize the photon beam delivered to the target after passing through all filters and reflecting off the back focusing mirror. Our spectrometer is based on a design from Kornilov *et al.*[25] with a modified geometry.

The XUV spectrometer is depicted in Figure 5. All components are mounted on a 7.0 x 3.6 inch aluminum breadboard that is attached to a custom DN160 CF cluster flange. The incoming high harmonics laser beam exits a differential pumping section through an alignment iris (F) and passes through the XUV-spectrometer unperturbed. After back-reflection off the focusing mirror in the end-station, the strongly diverging beam is refocused by a broadband mirror at a shallow angle (UV fused silica with broadband gold coating,

f = 10 cm). The mirror is mounted on a custom tip-tilt mount with minimal height in order to avoid interference with the incoming beam path. Tip and tilt of the mirror can be controlled manually using rotational feedthroughs that connect to the mount with flexible coupling wires. The focusing mirror is necessary to capture a sufficient amount of photons for a high quality spectrum. No slit was used in this geometry.

A transmission nano grating consisting of a Ta structure on a SiC membrane (200 nm pitch, 1.2 x 1.2 mm area, NTT AT) diffracts the harmonics onto a commercial multi-channel plate (MCP) photon detector mounted on a custom holder. A one inch diameter tube prevents stray light from illuminating the grating.

The photon detector ($\varnothing$ = 40 mm, Beam Imaging Solutions) consists of two resistance-matched micro-channel plates (MCPs) in a chevron configuration with an aluminum coated back stacked with a phosphor coated glass plate. The XUV photons generate an electron cloud in the channels of the MCPs that causes fluorescence of the phosphor screen. The diffraction pattern of the high harmonic light visible on the back side of the phosphor screen is imaged through a DN63 viewport behind the detector using a standard c-mount USB camera with a zoom lens. The strong zero-order laser beam transmitted through the grating is captured by a metal spiral that traps the photons and avoids illumination and damage of the MCPs. Furthermore, in order to reduce the amount of stray and background light falling on the imaging detector, the breadboard is enclosed inside a metal housing (not shown in the figure).

When the spectrometer is not in use, a copper plate blocks the back-reflected beam from entering the XUV-spectrometer. The plate prevents damage to the transmission grating as there is a sufficient amount of energy in the refocused infrared beam to destroy the grating. This is especially important when an intense infrared beam is used in the pump-probe experiment. The plate is rotated into the beam path using a feedthrough on the bottom of the chamber. It can also be used for a relative measurement of the high harmonics laser beam intensity by integrating the electric charge generated upon photon impact on the plate (read out via a Charge and Time Sensitive Amplifier CATSA, main amplifier, linear gate and stretcher, and pulse height to time converter).

The entire assembly is inserted vertically into a DN160 CF cross that is attached to the upstream entrance of the experimental end-station. The bottom flange holds the rotational feedthroughs for the mirror control and the beam block. Facing the spectrometer board, a

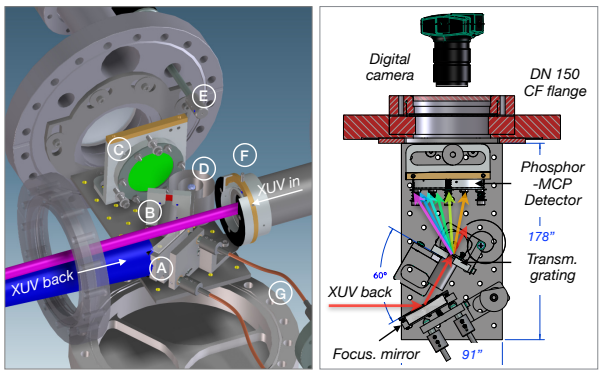

FIG. 5. (color online) Rendering of the compact XUV-spectrometer (left) and schematic view (right). (A) Re-focusing mirror, (B) nano-grating, (C) Phosphor-MCP detector, (D) Zero-order catcher, (E) manipulator for a non-magnetic alignment iris (F), flex couplings for manipulation of the focusing mirror.

large DN160 viewport allows observation of all components including the alignment iris.

Figure 3 shows a comparison of the XUV spectra of the harmonics beam recorded with this spectrometer after passing through a variety of solid and gas filters. The spatial expansion of the dispersed beam limits the spectral range to the harmonic orders 7 to 23. The relative intensity of different orders shows a rapid decrease in intensity above the 15^{th} harmonic. This corresponds to the photon energy dependent reflectivity of the B_4C multilayer coating used on the back-focusing mirror. However, the relative intensity is also affected by the different divergence of individual harmonics intrinsic to the HHG process. Low orders expand to beam sizes larger than the size of the collection mirror of the spectrometer which leads to a reduced signal intensity. Moreover, the varying detection efficiency of the MCP detector as a function of the light wavelength, as well as the angle dependent grating efficiency modify the spectrum to a certain degree. Further information can be found in[25].

D. Pump-Probe Interferometer

Most interferometers for time resolved studies introduce the pump-probe delay with a translation stage in the infrared arm outside of the vacuum environment. However, if pump and probe pulses are both in the VUV/XUV wavelength regime, an in-vacuum delay stage is required. Stability and ease of alignment were major concerns in the current design as coincidence studies at low repetition rates require long acquisition times. We therefore chose

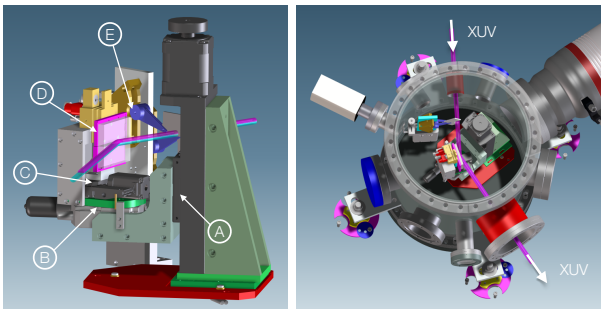

FIG. 6. (color online) Spit-Mirror Interferometer (SMI): (A) vertical translation stage, (B) rotational stage, (C) delay stage, (D) Tip-Tilt control of top mirror, (E) electrically actuated beam stops

a design where the Split-Mirror Interferometer (SMI) and the focusing optic are independent from each other. The interferometer is located upstream, while the focusing optic is placed inside the target chamber (see Fig 1). Using flat mirrors made of silicon at Brewster's angle for 800 nm (15° grazing angle) the intensity of the fundamental wavelength of the laser beam is reduced while maintaining relatively high reflectivity (~ 50 %) for the high harmonic XUV radiation.

Figure 6 shows renderings of the SMI and its position in a vibrationally isolated chamber. This design has several benefits in comparison to the alternative of a split back-focusing mirror geometry with translation of one of the mirrors as used elsewhere (e.g. see[20,26]). a) The shallow angle of the SMI mirrors with respect to the incident HHG beam converts the smallest delay stage step of 100 nm to a 170 as delay, a four times increased precision compared to a setup where the back-focusing mirror is translated. b) Pump and probe beams are focused by one solid mirror downstream from the SMI with both beams at roughly normal incidence. The overlap of both arms in the target is therefore inherent to the geometry and pointing instabilities do not affect the intensity significantly. c) The pump-probe overlap in time and space does not depend on the delay when using one solid mirror for back focusing. d) The ratio of the pump and the probe can be adjusted translating both mirrors together without moving the focus. Additionally, two metal plates can be moved quickly in and out of the beam using motorized arms in order to block each arm individually; this is very useful for setting up and tuning the experiment. The delay stage for introducing the delay on the bottom mirror (Micos active feedback) has a travel of about ± 8.5 ps (± 5 mm). At large delays, however, the focal quality is expected to degrade due to mirror astigmatism.

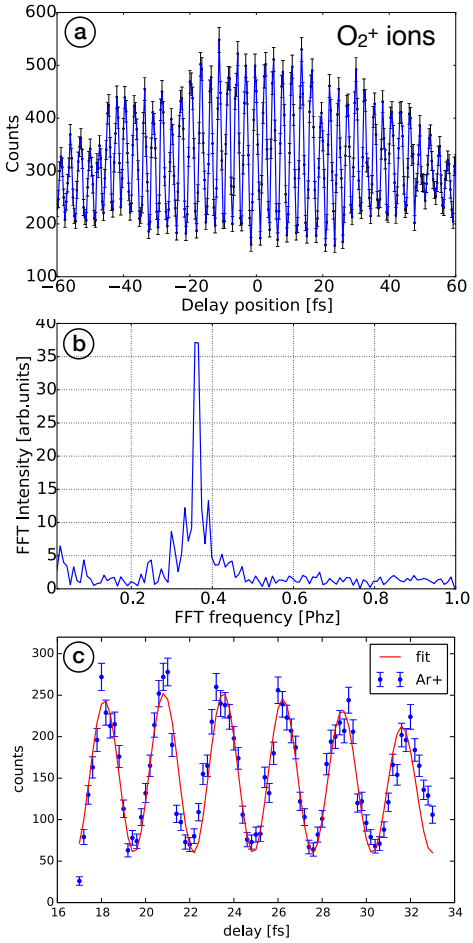

FIG. 7. (color online) (a) Pump-probe delay dependent yield of $O_2{}^+$ ions at 400 as step size from overlap of two infrared pulses. (b) Fourier transform spectrum corresponding to (a). (c) Ar^+ ion yield at 200 as step size.

Figure 7 shows the ionization yield from single ionization in oxygen (a) and argon (c) gas with respect to the pump-probe delay. Both measurements clearly show an oscillation corresponding to one optical cycle (2.67 fs) of the fundamental laser beam which is caused by interference of the IR field in the pump and the probe arms. The clear observation of this interference structure demonstrates the precision (200 as) and interferometric stability over a large range of delays of the Split-Mirror Interferometer.

E. COLTRIMS end-station

The COLTRIMS end-station consists of a versatile spectrometer for measuring the 3D-momenta of multiple particles in coincidence as well as a supersonic gas jet to provide an internally cold and spatially well-defined target. Figure 8 shows a schematic of the interior of the end-station with the spectrometer, the gas jet and the back-focusing mirror. A set of Helmholtz coils, which generate a static magnetic field, and a stack of copper electrodes, which establish several regions of electric fields, guide electrons and ions onto time and position sensitive detectors on both ends of the spectrometer. The spectrometer axis is parallel to the polarization direction of the high harmonics photon beam and perpendicular to the propagation direction of the gas jet as well as the polarization of the fundamental IR beam. The spectrometer is enclosed in an ultra-high vacuum chamber that is capable of pressures down to $6 \cdot 10^{-11}$ mbar. No magnetic materials were used in order to avoid distortion of the magnetic fields.

We use a curved mirror (f = 15 cm) to refocus the harmonic beam into the reaction zone. A shorter focal length which would yield higher intensity is not possible due to the size of the COLTRIMS spectrometer. For the 15^{th} harmonic we estimate a focus diameter of $< 10\ \mu m$. A precise calculation is difficult due to the unknown spatial profile of the HHG beam obtained after passing the various optics used in the beamline. The back-focusing mirror manipulator is mounted in line with the laser beam, preventing the XUV beam to be imaged directly. For alignment purposes, we have mounted two additional mirrors at 45° that can direct the infrared part of the beam through a viewport onto a camera. It should be noted, that the fundamental and harmonic orders can have a varying spatial profile due to different divergences.

1. Supersonic Gas Jet

The momentum uncertainty introduced by the thermal energy of the molecules at room temperature limits the energy and momentum resolution of particles from warm gas targets. Atomic and molecular beams, on the other hand, deliver much colder targets by converting the relative kinetic energy of atoms and molecules into a common directed motion via an adiabatic supersonic expansion[27]. We employ a two stage expansion scheme using a nozzle

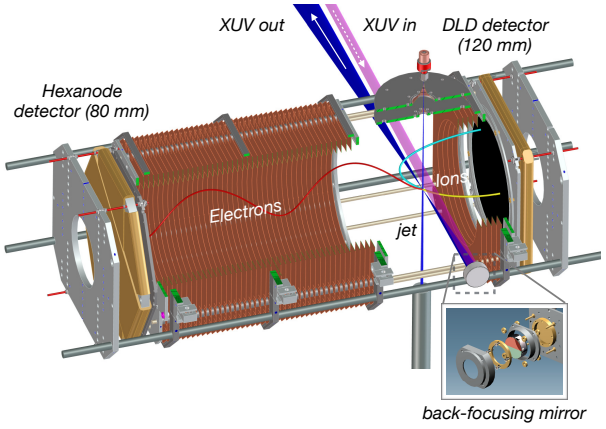

FIG. 8. (color online) Target zone inside the COLTRIMS end-station. The XUV-beam is back-focused into the gas jet inside the COLTRIMS spectrometer. Electrons and ions are collected by time and position sensitive detectors on opposite sides on a shot-by-shot basis.

with 30 μm orifice. The first skimmer extends into the region of the supersonic expansion also known as the "zone of silence" where particles have fully converted their relative kinetic energy into a directed propagation direction. The extent of this zone is defined by an equilibrium of the jet driving pressure and the local background pressure around it. At driving pressures of 50 - 200 psi with a turbo molecular pump (TMP) of 2000 l/s we choose distances of 7 to 12 mm between nozzle and skimmer (0.3 mm diameter) for maximal jet density. The second skimmer (0.5 mm diameter) limits the momentum uncertainty orthogonal to the propagation direction ($\sim$ 0.13 a.u.) and reduces the spatial target extension in this direction ($\sim$ 1.9 mm diameter in the reaction zone). However, the interaction region of the crossed laser beam and the gas target is usually defined by the laser focus for typical laser focus sizes of a few microns and Rayleigh ranges of less than 1 mm. The second expansion stage (670 l/s TMP speed) reduces the flow of background gas into the reaction chamber which is usually the most critical contribution to the background as it cannot be separated easily by gating on the time-of-flight. The jet passes through the interaction zone inside the spectrometer and leaves the main chamber through two differentially pumped stages. For an H_2 jet at 100 psi driving pressure we observe a pressure of 1.9×10^{-3} mbar in the source chamber, 3.5×10^{-6} mbar in the second jet stage and a pressure rise of 1.3×10^{-7} mbar in the jet dump. The contribution from the flow of warm background gas into the reaction chamber is on the order of 2×10^{-10} mbar. We estimate a target density of about 9×10^{10}

molecules/cm^2 for these gas jet conditions.

2. Spectrometer and Detectors

The 3D-momenta of electrons and ions can be retrieved by measuring the position of impact on the detectors and the time-of-flight of each particle. The spectrometer is built from an evenly spaced stack of thin copper plates that are connected with a chain of resistors. Applying a DC voltage creates a homogeneous electric field which drives ions and electrons onto the position sensitive detectors on the opposite sides of the spectrometer. Our momentum imaging spectrometer was designed to allow for a variety of experiments with different electron and ion energies. Ions and electrons can be measured on either detector side by adjusting spectrometer and detector voltages accordingly. We chose a geometry where the spectrometer is divided into one short side with a single acceleration region of 7.1 mm and one long side with a 6.8 mm and a 23.4 mm section. The resistor chain and the potential of several plates of the spectrometer can be adjusted via electrical feedthroughs to allow for pulsing specific plates or implementing electrostatic lenses. The plates around the interaction region have openings for the gas jet as well as the laser beam. The short side of the spectrometer is equipped with a 120 mm multi-channel plate detector (MCP) with dual-layer delay lines for time and position readout while the longer side has an 80 mm three layer (Hex) MCP delay line detector mounted. For more information on the resolution and capabilities of the large multi-hit capable time and position sensitive detectors see RoentDek GmbH[28].

III. BENCHMARK MEASUREMENTS

A. Argon Electron-Ion Coincidences

In order to demonstrate the coincidence detection capabilities of the setup, we have used the 11^{th}, 13^{th} and 15^{th} harmonic (selected using a tin filter) to ionize argon gas. Ions and electrons were measured in coincidence on their two respective detectors. Figure 9 (a) shows the z-component (time-of-flight direction) of the sum vs the difference of the electron and ion momenta. With no additional particle or momentum exchange involved, the momenta of the photo-electron and the ion from a single ionization are equal opposite due

to momentum conservation, equivalent to a constant sum momentum. Hence, electron-ion coincidences appear as a vertical line in the spectrum. By selecting only events with near zero momentum sum, an efficient data sorting filter is created to separate coincidence events from the background. The photoelectron energy spectrum (b) shows peaks corresponding to the ionization of the $^1S_0$ ground state of the Ar^+ ion (15.76 eV) using the three selected photon energies 17.1, 20.2 and 23.3 eV. Figures 9 (c) and (d) show slices through the 3D-momentum sphere in the detector plane (x-y) and the time-of-flight direction (z) vs the jet-direction (y). The three discrete electron energies form rings in momentum space that are distinct along the z-direction, which is equivalent to the polarization axis of the electric field of the XUV beam, hence, they reflect the dipole character of the absorbed photon beam. The spectra are selected using the described coincidence condition and the yield (linear color scale) is normalized according to the available solid angle of the different momenta ($p_i/p < cond.$ where p is the total momentum).

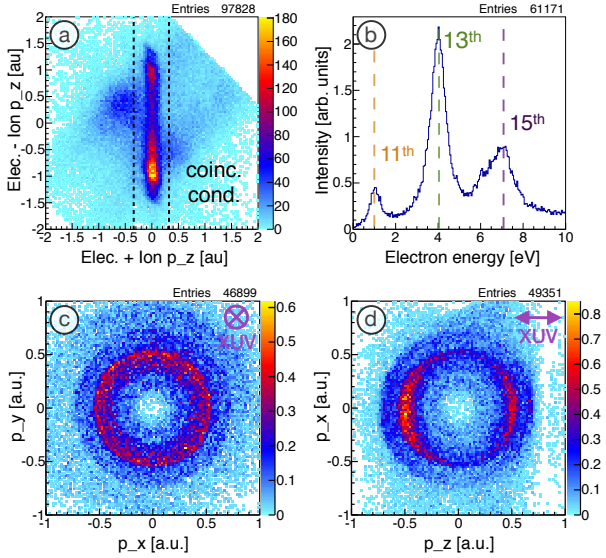

FIG. 9. (color online) Electron-ion coincidences from the ionization of argon using the 11^{th}, 13^{th}, and 15^{th} harmonic. (a) Z-components of ion versus electron momenta. The dashed line represents the boundaries for the coincidence software gate. (b) Electron energy spectrum. (c) x-y slice through the measured 3D-momentum sphere of the electron and (d) the corresponding z-y components (yield, i.e. linear color scale, is normalized according to the solid angle). The three photon energies appear as distinct rings in the electron momenta as the ionization occurs from a single electronic state (compare with (b)).

B. High Resolution Ion Momenta from Oxygen Dissociation

The advantages of a full 3D-momentum measurement as well as the extraordinary resolution of this setup are demonstrated in a measurement of molecular oxygen dissociation. A diagram of the potential energy curves of the $O_2{}^+$ cation is shown in Figure 10. The 13^{th} and the 15^{th} harmonic (20.2 and 23.3 eV) were used to excite oxygen to several excited states of the $O_2{}^+$ ion above the first dissociation limit (L1) at 18.73 eV that are known to dissociate through non-adiabatic coupling[29].

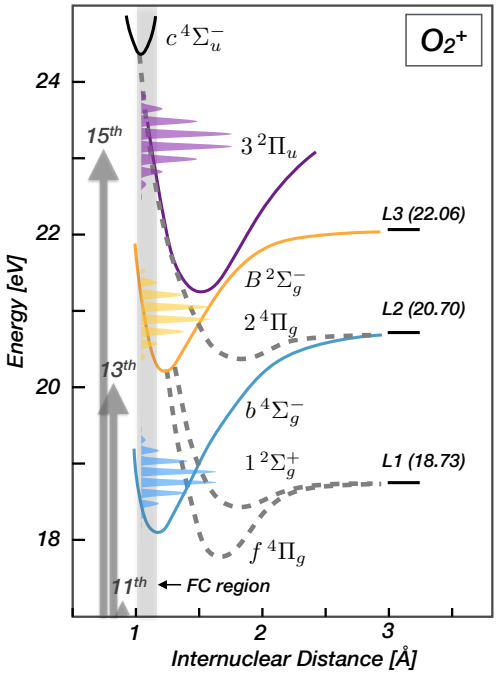

FIG. 10. (color online) Potential energy diagram of the relevant states of the $O_2{}^+$ cation (data taken from Lu et al.[30]). The length of the vertical arrows mark the photon energies of the high harmonic laser pulses.

Figure 11 (a) shows the measured ion time-of-flight (TOF) spectrum. Due to the intense photon beam(s) and the moderate vacuum conditions of 8×10^{-9} mbar, many peaks appear that are caused by the ionization and fragmentation of the oxygen molecule and many other residual gas contributions present in the chamber (i.e. hydrogen, water, nitrogen etc.). The TOF vs position spectrum in Figure (b) demonstrates how the complete 3D-measurement can be used to clearly distinguish even overlapping contributions of different fragments to the measured signals and hence demonstrates the power of differential measurements for

analysis and interpretation of the data generated by very intense photon sources such as HHG and FEL.

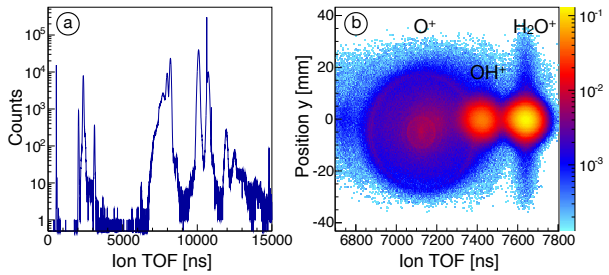

FIG. 11. (color online) (a) Ion time-of-flight (TOF) spectrum with a variety of peaks corresponding to the ionization of the O_2 target and residual gases in the chamber. (b) In the position vs. TOF spectrum the origin of the various ionization processes can be clearly distinguished between the target and background gas.

Figure 12 shows the reconstructed momenta of O^+ ions along p_z vs $p_{xy} = \sqrt{p_x^2 + p_y^2}$ direction (positive momenta only, mirrored at $p_z = 0$ to eliminate the contributions from overlapping OH^+ ions as seen in Fig.11 (b). The corresponding ion energy distribution is shown below (b). The kinetic ion energy integrated for all events is shown as a black line, the energy for ions emitted along the z-direction, i.e. the TOF direction which has the best resolution in our setup, is shown in blue. The series of sharp peaks can be attributed to the dissociation of metastable states of the ${O_2}^+$ cation: Photons from the 13^{th} laser harmonic create wave packets in the $b\,^4\Sigma_g^-$ state. Starting at $v' = 4$, the excited ${O_2}^+$ can dissociate by coupling to the $f\,^4\Pi_g$ and $^4\Sigma_g^+$ states that dissociate into the limit L1 forming the peak series starting at 0.060 eV (labelled with 1)[31]. Similarly, the series of peaks starting at ion energies of 0.780 eV (3) result from the population of vibrational states of the $B\,^2\Sigma_g^-$ state of the ${O_2}^+$ cation that dissociates through the $f\,^4\Pi_g$ and $d\,^4\Sigma_g^+$ states. The two isolated peaks around 2 eV (4) result from the ionization of the first and second vibrational level of the $c\,^4\Sigma_u^-$ state followed by the dissociation to limit L2 at 20.70 eV[29,32]. Dissociation to L1 and L5 (23.75 eV, not shown) has also been observed before[31] and likely contributes to the spectrum at 2.9 (5) and 0.4 eV respectively. As this state can only be populated at photon energies above 24.4 eV, we attribute this contribution to leakage of the 17^{th} and higher order harmonics through the filter. A broader peak around 0.5 eV (2) can result from the direct ionization and dissociation of the $2\,^4\Pi_g$ state to limit L2.

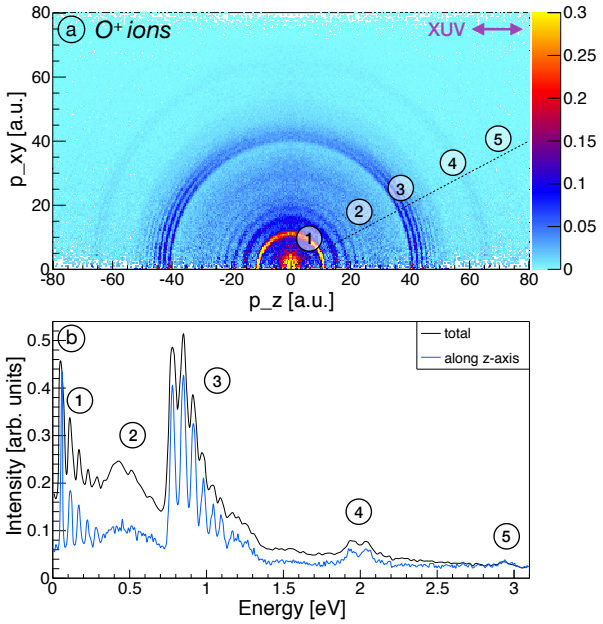

FIG. 12. (color online) Dissociative ionization of oxygen molecules using 17.1, 20.2 and 23.2 eV photons. (a) O^+ momentum parallel (p_z) vs perpendicular to the polarization direction of the high harmonics of the laser beam (symmetrized to $p_z = 0$). (b) Ion energy spectrum of the O^+ ions recorded. The sequences of sharp peaks around 0.1 and 0.8 eV correspond to the dissociation of metastable states of the $O_2{}^+$ cation (see text).

Figure 12 displays a very high kinetic energy resolution, exceeding similar previous experiments (see i.e. Siu *et al.*[33]). Based on a comparison with high resolution electron spectroscopy data from Baltzer *et al.*[29], we estimate an energy resolution of 43 meV (1.53×10^{-3} a.u.) at 0.8 eV ion energy. This can be explained by two aspects. Firstly, the laser focus of only a few microns creates a well-defined reaction source in the time-of-flight direction (z) and the jet-direction (y). Secondly, the thermal momentum uncertainty of the molecular gas jet perpendicular to its propagation direction (x) is minimal due to the use of the two skimmers (see Section II E 1). In the z-direction, both conditions apply combined with high detection resolution at an electric extraction field of 20.3 V/cm resulting in the observed spectral resolution. This is, to the best of our knowledge, the first apparatus that combines ultrafast XUV sources and advanced electron/ion 3D-momentum imaging with such a high energy and temporal resolution.

IV. CONCLUSION AND OUTLOOK

In this work we have presented a coincidence 3D-momentum imaging setup for time-resolved studies of molecular dynamics with a tabletop high energy photon source. Key features of the high harmonic beamline are independently energy- and time-selected pump and probe arms for time-resolved studies with photon energies entirely in the VUV and XUV regime enabled by a novel split-mirror interferometer.

Our HHG source delivers 10-20 fs long attosecond pulse trains in a spectral range from $\sim 5 - 50\,eV$. The pulse pairs can be delayed with a precision of 170 as and over a range of several picoseconds. Multiple gas, metal, and glas filters allow for an individual selection of the photon energy in each arm to form multi-color pulse pairs. The resulting spectrum can be analyzed using an ultra-compact XUV-spectrometer. Our COLTRIMS type 3D-Momentum imaging spectrometer in combination with a supersonic molecular gas jet provides high energy resolution and enables electron and ion coincidence measurements. These unique capabilities of a COLTRIMS type reaction microscope in combination with a coherent VUX/XUV light source were demonstrated in Argon electron-ion coincidence and oxygen high resolution ion measurements.

The apparatus presented here illustrates that table top XUV sources based on High Harmonic Generation in combination with 3D-momentum imaging spectroscopy can be used as an important tool for the time-resolved investigation of molecular dynamics on femtosecond time-scales. New developments of HHG sources and advances in laser technology could further improve the presented technique. A HHG source with a higher source photon flux would permit the implementation of a time compensated monochromator that enables a precise selection of the photon energy while retaining a pulse width of tens of femtoseconds, despite the significant photon losses in such devices. High power laser systems at kHz repetition rates have become available recently. Their future implementation with setups such as presented in this work will expand time-resolved 3D-imaging spectroscopy of molecular targets to highly differential VUV-XUV pump probe experiments and enable complex multi-fragment imaging studies that are presently inhibited by low laser repetition rates.

ACKNOWLEDGMENTS

We acknowledge many fruitful discussions and advice from R. Dörner, M. S. Schöffler and L. Ph. Schmidt. We are indebted to O. Jagutzki and A. Czasch from Roentdek GmbH and T. Jahnke from Cronologic GmbH for outstanding support for their momentum imaging detectors, readout, and software. Champak Khurmi, James Cryan and Elio Champenois gave valuable support with the laser system. R. Lucchese provided $O_2{}^+$ PEC. We thank the Center for Xray Optics (CXRO) for support with the design of the SMI as well as providing multilayer coated optics. F. S. acknowledges financial support by Studienstiftung des deutschen Volkes. This work was supported by the Director, Office of Science, Office of Basic Energy Sciences, and by the Division of Chemical Sciences, Geosciences, and Biosciences of the U.S. Department of Energy at LBNL under Contract No. DE-AC02-05CH11231.

REFERENCES

[1]G. D. Scholes, G. R. Fleming, A. Olaya-Castro, and R. van Grondelle, Nature Chemistry **3**, 763 (2011).

[2]D. Polli, P. Altoè, O. Weingart, K. M. Spillane, C. Manzoni, D. Brida, G. Tomasello, G. Orlandi, P. Kukura, R. A. Mathies, M. Garavelli, and G. Cerullo, Nature **467**, 440 (2010).

[3]H. Satzger, D. Townsend, M. Z. Zgierski, S. Patchkovskii, S. Ullrich, and A. Stolow, Proceedings of the National Academy of Sciences **103**, 10196 (2006).

[4]W. Ackermann *et al.*, Nature Photonics **1**, 336 (2007).

[5]P. Emma *et al.*, Nature Photonics **4**, 641 (2010).

[6]E. Allaria and and others, Nature Photonics **6**, 699 (2012).

[7]P. M. Paul, E. S. Toma, P. Breger, G. Mullot, F. Augé, P. Balcou, H. G. Muller, and P. Agostini, Science **292**, 1689 (2001).

[8]T. Brabec and F. Krausz, Reviews of Modern Physics **72**, 545 (2000).

[9]P. B. Corkum, Physical Review Letters **71**, 1994 (1993).

[10]Y. Nabekawa, T. Shimizu, T. Okino, K. Furusawa, H. Hasegawa, K. Yamanouchi, and K. Midorikawa, Physical Review Letters **96**, 083901 (2006).

[11]M. Hentschel, R. Kienberger, C. Spielmann, G. A. Reider, N. Milosevic, T. Brabec,

P. Corkum, U. Heinzmann, M. Drescher, and F. Krausz, Nature **414**, 509 (2001).

[12]T. Popmintchev, M.-C. Chen, P. Arpin, M. M. Murnane, and H. C. Kapteyn, Nature Photonics **4**, 822 (2010).

[13]E. Takahashi, Y. Nabekawa, T. Otsuka, M. Obara, and K. Midorikawa, Physical Review A **66**, 021802 (2002).

[14]P. Tzallas, D. Charalambidis, N. A. Papadogiannis, K. Witte, and G. D. Tsakiris, Nature **426**, 267 (2003).

[15]J. Ullrich, R. Moshammer, A. Dorn, R. Dörner, L. P. H. Schmidt, and H. Schmidt-Böcking, Reports on Progress in Physics **66**, 1463 (2003).

[16]P. Ranitovic, X. M. Tong, B. Gramkow, S. De, B. DePaola, K. P. Singh, W. Cao, M. Magrakvelidze, D. Ray, I. Bocharova, H Mashiko, A. Sandhu, E. Gagnon, M. M. Murnane, H. C. Kapteyn, I. Litvinyuk, and C. L. Cocke, New Journal of Physics **12**, 013008 (2010).

[17]E. Gagnon, A. S. Sandhu, A. Paul, K. Hagen, A. Czasch, T. Jahnke, P. Ranitovic, C. Lewis Cocke, B. Walker, M. M. Murnane, and H. C. Kapteyn, Review of Scientific Instruments **79**, 063102 (2008).

[18]S. J. Weber, B. Manschwetus, M. Billon, M. Böttcher, M. Bougeard, P. Breger, M. Géléoc, V. Gruson, A. Huetz, N. Lin, Y. J. Picard, T. Ruchon, P. Salières, and B. Carré, Review of Scientific Instruments **86**, 033108 (2015).

[19]E. Takahashi, Y. Nabekawa, H. Mashiko, H. Hasegawa, A. Suda, and K. Midorikawa, IEEE Journal of Selected Topics in Quantum Electronics **10**, 1315 (2004).

[20]T. K. Allison, T. W. Wright, A. M. Stooke, C. Khurmi, J. van Tilborg, Y. Liu, R. W. Falcone, and A. Belkacem, Optics Letters **35**, 3664 (2010).

[21]L. Poletto, P. Villoresi, E. Benedetti, F. Ferrari, S. Stagira, G. Sansone, and M. Nisoli, Journal of the Optical Society of America B **25**, B44 (2008).

[22]T. K. Allison, J. van Tilborg, T. W. Wright, M. P. Hertlein, R. W. Falcone, and A. Belkacem, Optics Express **17**, 8941 (2009).

[23]J. C. Rife, T. W. B. Jr, W. R. Hunter, and R. G. Cruddace, Physica Scripta **41**, 418 (1990).

[24]CXRO, "Center for X-Ray Optics," (2015).

[25]O. Kornilov, R. Wilcox, and O. Gessner, Review of Scientific Instruments (2010).

[26]Y. H. Jiang, T. Pfeifer, A. Rudenko, O. Herrwerth, L. Foucar, M. Kurka, K. U. Kühnel, M. Lezius, M. F. Kling, X. Liu, K. Ueda, S. Düsterer, R. Treusch, C. D. Schröter,

R. Moshammer, and J. Ullrich, Physical Review A **82**, 041403 (2010).

[27]H. Pauly, *Atom, Molecule, and Cluster Beams I*, Springer Series on Atomic, Optical, and Plasma Physics, Vol. 28 (Springer Berlin Heidelberg, Berlin, Heidelberg, 2000).

[28]RoentDek, "RoentDek Handels GmbH," (2015).

[29]P. Baltzer, B. Wannberg, L. Karlsson, M. Carlsson Göthe, and M. Larsson, Physical Review A **45**, 4374 (1992).

[30]Y. Lu, Z. He, J. Cutler, S. Southworth, W. Stolte, and J. Samson, Journal of Electron Spectroscopy and Related Phenomena **94**, 135 (1998).

[31]T. Akahori, Y. Morioka, M. Watanabe, T. Hayaishi, K. Ito, and M. Nakamura, Journal of Physics B: Atomic and Molecular Physics **18**, 2219 (1985).

[32]A. Lafosse, J. C. Brenot, A. V. Golovin, P. M. Guyon, K. Hoejrup, J. C. Houver, M. Lebech, and D. Dowek, The Journal of Chemical Physics **114**, 6605 (2001).

[33]W. Siu, F. Kelkensberg, G. Gademann, A. Rouzée, P. Johnsson, D. Dowek, M. Lucchini, F. Calegari, U. De Giovannini, A. Rubio, R. R. Lucchese, H. Kono, F. Lépine, and M. J. J. Vrakking, Physical Review A **84**, 063412 (2011).